Topological defects in epithelia govern the extrusion of dead cells

Thuan Beng Saw[1,2,†], Amin Doostmohammadi[3,†], Vincent Nier[4], Leyla Kocgozlu[1], Sumesh Thampi[3,5], Yusuke Toyama[1,6], Philippe Marcq[4], Chwee Teck Lim[1,2,*], Julia M Yeomans[3,*], Benoit Ladoux[1,7,*]

[1]Mechanobiology Institute, National University of Singapore, Singapore
[2]National University of Singapore Graduate School of Integrative Sciences and Engineering (NGS), National University of Singapore, Singapore
[3] The Rudolf Peierls Centre for Theoretical Physics, Oxford University, UK
[4] Sorbonne Universités, UPMC Université Paris 6, Institut Curie, CNRS, UMR 168, Laboratoire Physico-Chimie Curie, Paris, France
[5] Department of Chemical Engineering, Indian Institute of Technology Madras, Chennai, India
[6]Department of Biological Sciences, National University of Singapore, and Temasek Life Sciences Laboratory, Singapore
[7]Institut Jacques Monod (IJM), CNRS UMR 7592 & Université Paris Diderot, Paris, France

† These authors contributed equally to this work.

*Corresponding authors

Prof. Chwee Teck Lim
Email: ctlim@nus.edu.sg

Prof. Julia M Yeomans FRS
Email: Julia.Yeomans@physics.ox.ac.uk

Dr. Benoit Ladoux
Email: benoit.ladoux@ijm.fr

Epithelia remove excess cells through extrusion whereby cells are pushed out of the monolayer, thus preventing accumulation of unnecessary or pathological cells. The extrusion process can be triggered by apoptotic signaling[1], oncogenic transformation[2-4], and overcrowding of cells[5-7]. Despite the important links of cell extrusion to developmental, homeostatic and pathological processes, including morphogenesis[8,9], epithelial turnover[6], bacteria invasion[10] and cancer metastasis[2,3,11], its underlying mechanism and connections to the intrinsic mechanical properties of the epithelium are largely unexplored. Here, using Madin-Darby canine kidney (MDCK) tissue as a model system, we show that apoptotic cell extrusion is provoked by singularities in cell alignments in the form of topological defects. We find a universal and robust correlation between the extrusion sites and positions of comet-like, nematic defects in the cell orientation field in several types of epithelium including human epithelial skin (HaCaT) and breast cell lines (MCF10a). We model the epithelial dynamics as an active nematic liquid crystal[12,13] and compare the numerical simulations to tissue strain rate measurements and stresses within cell monolayers[14]. The results confirm the active nematic nature of the epithelium and demonstrate that defect-induced isotropic stresses serve as the primary precursor of extrusions. Exploiting this defect-induced extrusion mechanism, we further demonstrate the ability to control extrusion hotspots by geometrically inducing nematic defects through microcontact-printing[15] of patterned tissue. Together we propose a novel mechanism for apoptotic cell extrusion: spontaneous topological defects in epithelial tissue govern cell fate. This new finding has important implications in predicting extrusion hotspots and dynamics *in vivo*, with potential applications to tissue regeneration and metastasis suppression. Moreover, we anticipate that the analogy between the dynamics of the epithelium and of active nematic liquid crystals will trigger further investigations of the link between cellular processes and the material properties of epithelia.

To understand the mechanisms that underlie apoptotic cell extrusion (Fig. 1a, b, c), we investigated the relationship between apoptotic cell extrusion and tissue remodeling within epithelial cell monolayers. By culturing MDCK epithelial cells at confluency on micropatterned substrates coated with extra-cellular matrix proteins (see Methods), we first observed that the cells in the dense tissue were anisotropic in shape over long periods of time (Extended Data Fig. 1a, b) and demonstrated supracellular orientational order in their alignment (Extended Data Fig. 1c, d). The ordering was destroyed at specific locations in the tissue by topological defects, singularities in the cellular alignment. There are mainly two types of topological defects in nematic liquid crystals, of topological charges +1/2 (comet-like) and -1/2, and both were identified in the tissue (Fig. 1d)[12].

Intriguingly, we found that extrusion events were strongly correlated to the positions of comet-like defects in the cell alignment (Fig. 1e, f – see Methods for details). In particular, extrusions predominantly occurred at the head region of the +1/2 defects (Fig. 1g). To investigate the universality and the robustness of the correlation between extrusion and +1/2 defects, we first examined the effect of mytomycin-c treatment on MDCK tissue to inhibit cell division and its possible effects, as division is known to be a source of activity and could generate perturbation in cell alignment in the tissue[16]. We then examined different epithelial tissues including human epithelial skin (HaCaT) and breast cell lines (MCF10a). In all cases, extrusions maintained strong correlation patterns with +1/2 defects (Fig. 1f) as in unperturbed MDCK tissue and less so to -1/2 defects (Extended Data Fig. 1e, f, g). We thus hypothesized that singularities in cellular alignment are spontaneously generated in epithelial tissues in the form of nematic topological defects, and the defects in turn trigger cell apoptosis and extrusion.

To probe the first part of the hypothesis, we studied the properties of singular points of cellular alignment in wild-type (WT) MDCK to confirm their identification with topological defects in active nematic liquid crystals. We used Particle Image Velocimetry[17] (PIV - see Methods) to measure experimentally the velocity and strain rate fields around the singular points in cell alignment (Fig. 2a, b, c), and compared them to numerical simulations (see Methods and Supplementary Information) of the tissue as active nematic liquid crystal (Fig. 2d, e, f)[16]. The close match between strain rate patterns and velocity fields around +1/2 topological defects in experiments and simulations (Fig. 2a, b, c and d, e, f) revealed that the tissue indeed behaves as an extensile, active nematic liquid crystal. The extensile nature of the cell activity is manifest as flows along the elongated axes of the cells that move toward the head region of the defect (Fig. 2c, f). MDCK tissue in other conditions that we tested (mytomycin-C and blebbistatin) also exhibited similar velocity field maps as the extensile active nematic model (Extended Data Fig. 2a, b). Moreover, active nematic theory predicts that the defect density scales proportionally with the activity of the tissue[13,18]. We tested this by introducing blebbistatin treatment (10 μM) to reduce the actomyosin activity, as active stresses in the tissue originate to a large extent from the actomyosin activity[19]. The measurements indeed showed a significant drop in the defect density compared to normal conditions (Extended Data Fig. 2c). These results further demonstrate that the epithelium is behaving as an active nematic liquid crystal and topological defects are spontaneously formed by active stresses in the tissue.

From liquid crystal theory, the spontaneously formed topological defects are expected to generate mechanical stress in their vicinity[20]. Further, since recent studies showed that mechanical stress plays a role in cell extrusion[5-7], we hypothesized that the presence of +1/2 defects led to a stress distribution that favored apoptotic cell extrusions in epithelial tissues. To test this hypothesis, we measured mechanical

traction exerted by cells on the underlying substrate (Fig. 2g) with Traction Force Microscopy[21] (TFM - see Methods), and converted the traction to two-dimensional stress, $\boldsymbol{\sigma}$ in the tissue (Fig. 2h) using Bayesian Inversion Stress Microscopy[14] (BISM - see Methods). First, the close resemblance of the stress maps (Fig. 2i, j) and the strain rate (Fig. 2a, b) in our results show that, at least in the vicinity of +1/2 defects MDCK tissue acts predominantly as a viscous fluid rather than an elastic material as stated by previous studies[22], suggesting that cells can flow more easily near +1/2 defects. Then, consistent with the velocity field results, the stress pattern around +1/2 defects in the experimental measurements is again highly similar to that in extensile nematic simulations (Fig. 2i, j and k, l).

To understand the mechanistic basis for the correlation between extrusion events and comet-like defects, we calculated the isotropic contribution to the stress around cells that were going to extrude and around topological defects (Fig. 3a,b). The isotropic stress provides a clear distinction between the two defects as it is only highly compressive (negative) at the head portion of a +1/2 defect, while being largely tensile at a -1/2 defect (Fig. 3a, b). Consistently, these unique isotropic stress distributions are reflected in the simulations (Fig. 3c, d). In addition, we measured the isotropic stress for cells that were going to extrude. Interestingly, the time evolution of the isotropic stress around these cells showed that they are increasingly being compressed (increasingly negative isotropic stress with time - Fig. 3e, f) in the time leading up to their extrusion. This rationalizes why extrusions occur preferentially near the head regions of +1/2 defects (Fig. 1g) and why extrusion events are more correlated with +1/2 defects and less with -1/2 ones (Fig. 1e, f and Extended Data Fig. 1e, f, g). Finally, not all defect structures are correlated with extrusions, and we found that a critical compressive stress threshold has to be reached at +1/2 defects to induce cell extrusions (see Methods and Extended Data Fig. 3a).

To further prove the causal role of defects for extrusions, we sought to control defect locations in the tissue[18,23]. Since MDCK cells preferentially align tangential to a boundary between tissue-adherent and non-adherent substrates[17], we microcontact-printed (see Methods) a star-shaped tissue (Fig. 4a) to geometrically force comet-like defects to the four tips of the star. The length scales of the tip of the star ($\sim$ 100 - 200 μm) was chosen to match the size of the defects. We indeed found that the defect density increased at the corners of the star and that subsequently extrusions predominantly happened close to the four tips of the geometry (Fig. 4b, c). In contrast, the -1/2 defect density became larger near the center of the star (Fig. 4c), but there was no increase in extrusion events in this region. This biased distribution of extrusions was not found in a circular-shaped tissue (Fig. 4d, e, f). Thus we demonstrated that cell apoptosis and extrusion can be controlled by artificially controlling the positions of +1/2 defects in the tissue.

These findings reinforce the idea that comet-like defects in cellular tissue can mechanically induce cell extrusions. However, one may ask the reverse question: can apoptotic cells destined for extrusion produce certain biochemical signals that can increase tissue activity[1,3,22] and hence generate new local defects to expedite their own extrusion? To challenge the possibilities that apoptotic cells can promote local defect formation to expedite their subsequent extrusion (through biochemical signaling to increase tissue activity[1,3]), we used UV laser to induce a single cell apoptosis[9] (see Method) and followed the time evolution of the number of +1/2 defects immediately afterward (within a radius of 80 μm - Fig. 4g) up to several hours, till the first extrusion occurred. We could not find any evidences for the influence of apoptotic signaling on triggering more defects (Fig. 4h).

Taken together, our results show that as cells collectively move in the tissue, defects in cell alignments with high orientational elasticity are formed spontaneously. The emergence of defects provides hotspots of compressive stress, which lead to a higher probability of cell apoptosis and extrusion (Fig. 4i). The existence of a stress threshold suggests that the role of stress is to eject cells mechanically, but the possibility that stress triggers a signaling pathway leading to extrusion is not ruled out by our observations (caspase activity during extrusion – Fig. 1c). The identification of this mechanism allows tuning of extrusion hotspots through the control of topological defects in the tissue[18,23]. Notably, the magnitude of the measured critical compressive stress needed for extrusion is modest (~ 250 - 350 Pa.μm or ~ 50 - 70 Pa taking the typical cell height to be ~ 5 μm – Extended Data Fig. 3a) compared to other measured stress values in 2D and 3D tissues[24-26], suggesting that mechanical activation of extrusions and other mechano-transducable cell activities could be triggered not just in extreme physical environments or niches (e.g. extremely curved substrate surfaces, overcrowding[5-7,27]). We conclude that the spontaneous formation of singularities in cellular alignment in the form of nematic topological defects, is a previously unidentified cause of cell apoptosis, suggesting that such defects govern cell fate. Hence, it is anticipated that the defect-induced extrusion mechanism could be a common strategy for preserving homeostasis of a normal epithelium *in vivo* and for suppressing tumor invasion. It would be interesting to explore the role of topological defects in pathological conditions including oncogenic cell extrusion.

Acknowledgements
The authors thank Shreyansh Jain, René-Marc Mège and group members from MBI for helpful discussions. Financial supports from the Human Frontier Science Program (grant RGP0040/2012), the European Research Council under the European Union's Seventh Framework Program (FP7/2007-2013) / ERC grant agreements n° 617233 (BL) and n° 291234 (JMY) and the Mechanobiology Institute are gratefully acknowledged. T.B.S. is supported by an NGS scholarship.

Author Contributions
T.B.S., A.D., J.M.Y. and B.L. designed research, T.B.S., L.K., Y.T. performed experiments, A.D., S.T. implemented the numerical method and did the *in silico* simulations, T.B.S., A.D., V.N., P.M. contributed new reagents, modeling and computational tools, T.B.S., A.D., J.M.Y. and B.L. wrote the paper, C.T.L, J.M.Y. and B.L. supervised the project. All authors read the manuscript and commented on it. Authors do not have conflict of interests to declare.

Methods

Cell culture and reagents

MDCK strain II WT and HaCaT (Cell Lines Service) cells were maintained in a culture medium composed of high glucose DMEM 1X medium (Invitrogen), 100 μg/ml penicillin, 100 μg/ml streptomycin (Invitrogen), and 10% fetal bovine serum (Invitrogen). Culture medium for MDCK with stable GFP-actin was additionally supplemented with 250 μg/ml geneticin (Invitrogen). MCF10a cells were maintained in MEGM (Lonza) medium supplemented with cholera toxin (100 ng/ml). All cells were grown at 37 °C and 5% CO_2. For microscopy imaging, DMEM was replaced with low glucose Leibovitz (Sigma-Aldrich). MCF10A imaging was done in its culture medium. To reduce tissue acto-myosin activity, blebbistatin (Selleckchem) was added at 10 μM for 1 hr before imaging. To inhibit MDCK proliferation, mytomycin-C (Sigma) was added at 10 μg/ml for 1 hr, and rinsed before imaging. For live imaging of fluorescent cell nuclei, the confluent monolayer was incubated with Hoechst at 1 μg/ml for 5 min and rinsed. To monitor cell

viability in experiments, caspase-3 indicator NucView (Abcam) was added in the medium at 1:1000 dilution for 1 hr before imaging.

Microscopy imaging

A mature and confluent monolayer was allowed to develop overnight before experiments started. Typical experiments were run for 1 - 2 days. Phase contrast and fluorescence time-lapse imaging for tissue on a glass-bottom petri dish, PDMS spin-coated dish, and TFM soft gel were performed using a Biostation (Nikon) or Olympus 1X2-UCB inverted microscope. Confocal time-lapse images were obtained on a Nikon A1R MP laser scanning microscope or Zeiss upright Z2 microscope.

Microcontact printing

Silicon wafers with desired patterns were made using SU-8 photoresist for soft lithography[15]. To form stamps, PDMS (Sylgard 184, Dow Corning) at 1:10 mixture ratio (curing agent: silicone elastomer) was molded onto silanized wafers and cured at 80 °C for 2 hr. A mixture of 50 μg/ml pure fibronectin (Roche) and 25 μg/ml conjugated fibronectin (Cy5.5 or Atto dye, GE Healthcare and Sigma) was incubated on the stamps for 1 hr and dried before stamping. Patterns were stamped onto a UV-activated, PDMS spin-coated petri dish and the unstamped area was passivated by 1% Pluronics (F127, Sigma) for 1 hr. Samples were rinsed with PBS before cell seeding.

Traction Force Microscopy (TFM)

Soft silicone gel attached with fluorescent beads was used as substrate for TFM so that in-plane cell traction forces on the substrate could be measured[28]. To prepare the gel with a stiffness of 10 - 20 kPa, CyA and CyB components (Dow Corning) were mixed at 1:1 ratio and spin-coated on a petri-dish to achieve a flat substrate of height ~60 - 100 μm. After curing at 80°C for 2hr, the substrate was silanized with 5% (3-Aminopropyl) trimethoxysilane (Sigma) in ethanol for 5 min. Carboxylated fluorescent beads (100 nm, Invitrogen) were functionalized on the substrate at 1:500 dilution in DI water. The beads were passivated with 1X Tris (Sigma) for 10 min and pure fibronectin (50 μg/ml) was incubated on the substrate for 1 hr prior to cell seeding. Bead displacements acquired during experiments were measured and converted to cell traction forces with an ImageJ plugin[29].

Cell apoptosis induction

Laser induction of cell apoptosis[9] was done on a Nikon A1R MP laser scanning confocal microscope with Nikon Apo 60x/1.40 oil-immersion objective. An ultraviolet laser (355 nm, 300ps pulse duration, 1 kHz repetition rate, PowerChip PNV-0150-100, Teem Photonics) was focused on the nucleus of a target cell for 10 s at a laser power of 25 nW at the back aperture of the objective.

Image Analysis

Cell extrusion and apoptosis determination

The typical geometry of an extruded cell as a protrusion out of the relatively flat epithelial monolayer allowed simple and clear detection of the extrusion under phase contrast or bright field imaging (the extrusion appears as a bright spot). In fluorescence microscopy, extrusion is marked by the disappearance of the nucleus. The first frame where the extruding cell started to adopt a distinct morphology from its neighbor cells was defined as the time of initiation of extrusion. All extruding cells checked for viability displayed clear caspase-3 activation simultaneously with the initiation of extrusion, showing that the extrusions were apoptotic extrusions (Fig. 1c).

Automated nematic characterization of experimental images

To obtain the nematic director (orientation) field in a tissue, a clear epithelial tissue image (which can be phase contrast or fluorescence image) was obtained, with individual cell boundaries visible to the eye (Extended Data Fig. 4b Step 1). The image was smoothed using Bandpass Filter in ImageJ to remove unnecessary details (Extended Data Fig. 4b Step 2). The filter size of small structures was set to roughly one-third the size of a single cell. The ImageJ plugin, OrientationJ was used to detect the direction of largest eigenvector of the structure tensor of the image[30] for each pixel (for window size of roughly one quarter of size of single cell), outputted as gray-values from -90° to +90° (Extended Data Fig. 4b Step 3). The local nematic order parameter tensor, Q[20] was calculated (the nematic window size averages over pixel directions in a fixed-size region that contained 3 - 5 cells) for each point on a grid that discretized the image, using an in-house Matlab code. The grid distance was 75% of the nematic window size. Only pixels that resided in the region of the cell body were taken into account for this calculation (white regions obtained by Auto Local Threshold function in ImageJ, Extended Data Fig. 4b Step4) as cell boundary regions could have orientations that are perpendicular to the cell body. The largest eigenvector of Q was taken to be the local orientation of 3 - 5 cells, and plotted (red lines) over the original image for inspection (Extended Data Fig. 4b Step 5). Once the nematic director field was established, automatic nematic defect detection was done based on calculation of winding number[31]. Only two types of defects (+1/2 and -1/2) were predominantly found. To reduce false positives, only stably detected defects (i.e. defects found in at least two consecutive frames at the same location) were considered for further analysis. To determine a measure for the global ordering of the tissue, the order parameter, S[20] (Extended Data Fig. 1c) for all local regions (which can incorporate ~ 16 nematic directors each) throughout the tissue was averaged.

Cell Aspect Ratio calculation

The shape of cells in typical phase contrast images was tracked in Matlab using Fogbank software[32]. The cell shape for several images were manually traced to verify the results.

Particle Image Velocimetry (PIV)

The velocity field in 10X, phase contrast tissue time-lapse images was obtained using an open source Matlab code (PIVlab[33]), with three-passes (64*64, 32*32, and 16*16 pixel size interrogation window with 50% overlap each). The interrogation window sizes were scaled accordingly for higher magnification images.

Part III: Calculation of physical quantities: Extrusion-Defect correlation

For each extrusion, the distance, r to its closest defect in the preceding frame was determined and a normalized probability distribution function (pdf) for r was plotted. A similar pdf was also obtained for random points generated in the space of the tissue. The relative pdf was calculated by taking the difference between the extrusion-defect pdf and the random point-defect pdf, and could have positive or negative values. n = 30 (different sets of random points for each relative pdf). A relative pdf which showed a higher spatial correlation between extrusion and defect would have larger positive values at $r \sim 0$ μm. The measure of the strength of the extrusion-defect correlation is thus taken as the sum of the two points closest to the origin in the relative pdf.

Strain rate and stress measurements

Strain rate was calculated using the formula, $E_{ij} = (\partial_i u_j + \partial_j u_i)/2$, with $i, j \in (x, y)$ and velocity field, u_i obtained from PIV measurements. Stress was estimated from traction force data by inversing the force balance equation[14]. This underdetermined problem was solved by Bayesian inversion from the BISM method, independently of the epithelial rheology (see Supplementary Information for details). The stress estimate was defined

as the mode of the posterior stress pdf (maximal a posteriori estimate, see Supplementary Information for details). Isotropic stress was taken as the trace of the stress tensor, $(\sigma_{xx} + \sigma_{yy})/2$ in the tissue. Average strain rate and stress maps for the defects were calculated by rotating and aligning the defects to the y-axis at the origin, and averaging the values of the rotated vectors and matrices (in their new basis) for the corresponding pixel locations in all defects. Smoothing was done by linear interpolation of maps.

Critical extrusion stress

For each +1/2 defect, the shortest time to the next extrusion and the spatial distance of the defect core to this extrusion was determined. +1/2 defects were pooled into groups based on the values of the compressive isotropic stress at their head regions (area of 60*60 μm^2), and a heat map of the corresponding frequency of time and distances to the closest extrusions (for each defect group) was drawn. Hotspots in the heat maps for defect groups of tensile isotropic stress (positive) and lower compressive isotropic stress (less negative) are usually found at distances > ~ 200 μm and are more spread over time. In contrast, the hotspot for the heat map with stress < -250 Pa.μm localizes at time 0 min and at distance ~ 50 μm (Extended Data Fig. 3c). The latter is consistent with the position of the high compressive stress region in the +1/2 defect i.e. ~ 50 μm from the defect core. Thus, the 250 Pa.μm value defines the critical extrusion stress.

Active nematic simulation

The orientational dynamics of the monolayer and the defect properties were described by the equations of active nematohydrodynamics[34], which have proven successful in describing active systems[13,16,35,36]. Numerical simulations were performed using a hybrid Lattice-Boltzmann method to solve the hydrodynamic equations and calculate the orientational order of cells[16,34] (see Supplementary Information for details).

References

1 Rosenblatt, J., Raff, M. C. & Cramer, L. P. An epithelial cell destined for apoptosis signals its neighbors to extrude it by an actin-and myosin-dependent mechanism. *Curr. Biol.* **11**, 1847-1857 (2001).

2 Hogan, C. *et al.* Characterization of the interface between normal and transformed epithelial cells. *Nat. Cell Biol.* **11**, 460-467 (2009).

3 Wu, S. K. *et al.* Cortical F-actin stabilization generates apical–lateral patterns of junctional contractility that integrate cells into epithelia. *Nat. Cell Biol.* **16**, 167-178 (2014).

4 Wagstaff, L. *et al.* Mechanical cell competition kills cells via induction of lethal p53 levels. *Nat. Commun.* **7**, 122373 (2016).

5 Marinari, E. *et al.* Live-cell delamination counterbalances epithelial growth to limit tissue overcrowding. *Nature* **484**, 542-545 (2012).

6 Eisenhoffer, G. T. *et al.* Crowding induces live cell extrusion to maintain homeostatic cell numbers in epithelia. *Nature* **484**, 546-549 (2012).

7 Levayer, R., Dupont, C. & Moreno, E. Tissue Crowding Induces Caspase-Dependent Competition for Space. *Curr. Biol.* (2016).

8 Monier, B. *et al.* Apico-basal forces exerted by apoptotic cells drive epithelium folding. *Nature* **518**, 245-248 (2015).

9 Toyama, Y., Peralta, X. G., Wells, A. R., Kiehart, D. P. & Edwards, G. S. Apoptotic force and tissue dynamics during Drosophila embryogenesis. *Science* **321**, 1683-1686 (2008).

10 Pentecost, M., Otto, G., Theriot, J. A. & Amieva, M. R. Listeria monocytogenes invades the epithelial junctions at sites of cell extrusion. *PLoS Pathog.* **2**, e3 (2006).
11 Slattum, G. M. & Rosenblatt, J. Tumour cell invasion: an emerging role for basal epithelial cell extrusion. *Nat. Rev. Cancer* **14**, 495-501 (2014).
12 Marchetti, M. *et al.* Hydrodynamics of soft active matter. *Rev. Mod. Phys.* **85**, 1143 (2013).
13 Thampi, S. P., Golestanian, R. & Yeomans, J. M. Vorticity, defects and correlations in active turbulence. *Philos. T. Roy. Soc. A* **372**, 2029 (2014).
14 Nier, V. *et al.* Inference of internal stress in a cell monolayer. *Biophys. J.* **110**, 1625-1635 (2016).
15 Vedula, S. *et al.* Microfabricated environments to study collective cell behaviors. *Method Cell Biol.* **120**, 235-252 (2013).
16 Doostmohammadi, A. *et al.* Celebrating Soft Matter's 10th Anniversary: Cell division: a source of active stress in cellular monolayers. *Soft Matter* **11**, 7328-7336 (2015).
17 Vedula, S. R. K. *et al.* Emerging modes of collective cell migration induced by geometrical constraints. *Proc. Natl Acad. Sci.* **109**, 12974-12979 (2012).
18 Doostmohammadi, A., Adamer, M. F., Thampi, S. P. & Yeomans, J. M. Stabilization of active matter by flow-vortex lattices and defect ordering. *Nat. Commun.* **7**, 10557 (2016).
19 Prost, J., Jülicher, F. & Joanny, J. Active gel physics. *Nat. Phys.* **11**, 111-117 (2015).
20 de Gennes, P.-G. & Prost, J. The physics of liquid crystals. *Oxford University Press, USA*, 0.20 (1995).
21 Vedula, S. R. K. *et al.* Epithelial bridges maintain tissue integrity during collective cell migration. *Nat. Mater.* **13**, 87-96 (2014).
22 Serra-Picamal, X. *et al.* Mechanical waves during tissue expansion. *Nat. Phys.* **8**, 628-634 (2012).
23 Lopez-Leon, T., Koning, V., Devaiah, K., Vitelli, V. & Fernandez-Nieves, A. Frustrated nematic order in spherical geometries. *Nat. Phys.* **7**, 391-394 (2011).
24 Tambe, D. T. *et al.* Monolayer stress microscopy: limitations, artifacts, and accuracy of recovered intercellular stresses. *PloS One* **8**, e55172 (2013).
25 Campàs, O. *et al.* Quantifying cell-generated mechanical forces within living embryonic tissues. *Nat. Methods* **11**, 183-189 (2014).
26 Moussus, M. *et al.* Intracellular stresses in patterned cell assemblies. *Soft Matter* **10**, 2414-2423 (2014).
27 Boghaert, E. *et al.* Host epithelial geometry regulates breast cancer cell invasiveness. *Proc. Natl Acad. Sci.* **109**, 19632-19637 (2012).
28 Brugués, A. *et al.* Forces driving epithelial wound healing. *Nat. Phys.* (2014).
29 Martiel, J.-L. *et al.* Measurement of cell traction forces with ImageJ. *Method Cell Biol.* **125**, 269-287 (2015).
30 Rezakhaniha, R. *et al.* Experimental investigation of collagen waviness and orientation in the arterial adventitia using confocal laser scanning microscopy. *Biomech. Model Mechan.* **11**, 461-473 (2012).
31 Huterer, D. & Vachaspati, T. Distribution of singularities in the cosmic microwave background polarization. *Phys. Rev. D* **72**, 043004 (2005).
32 Chalfoun, J. *et al.* FogBank: a single cell segmentation across multiple cell lines and image modalities. *BMC Bioinformatics* **15**, 1 (2014).
33 Thielicke, W. & Stamhuis, E. J. PIVlab–Towards user-friendly, affordable and accurate digital particle image velocimetry in MATLAB. *J. Open Res. Softw.* **2**, e30 (2014).
34 Marenduzzo, D., Orlandini, E., Cates, M. E. & Yeomans, J. M. Steady-state hydrodynamic instabilities of active liquid crystals: Hybrid lattice Boltzmann simulations. *Phys. Rev. E* **76**, 031921 (2007).

35 Bittig, T., Wartlick, O., Kicheva, A., González-Gaitán, M. & Jülicher, F. Dynamics of anisotropic tissue growth. *New J. Phys.* **10**, 063001 (2008).
36 Volfson, D., Cookson, S., Hasty, J. & Tsimring, L. S. Biomechanical ordering of dense cell populations. *Proc. Natl Acad. Sci.* **105**, 15346-15351 (2008).

Figure Legends

Figure 1 | Extrusion correlates with specific singularities in cell orientation (+1/2 defects) in the epithelia.
a, Schematic of confluent monolayer and extruding cell (grey - cell body, blue - nucleus, orange - apoptotic extruding cell). **b,** Side view confocal image of confluent MDCK monolayer and extruding cell (green - actin, blue - nucleus). Scale bar, 10 μm. **c,** Corresponding images of activation of caspase-3 apoptotic signal (red). **d,** Schematic and experimental images of +1/2 defect (left) and -1/2 defect (right). The blue dot and arrow represent the defect core and tail-to-head direction of the +1/2 defect. Green triangle represents the -1/2 defect core. Red lines overlaid on the tissue are nematic directors denoting the average local orientation of several cells at each point. Scale bar, 10 μm. **e,** Schematic representation of how the correlation between extrusion and +1/2 defect is determined: the distance, r of each extrusion to its closest defect in the preceding frame is measured. **f,** Averaged relative probability distribution function (pdf) of r, for extrusion - defect pairs compared to that of random point - defect pairs (see Methods, Extrusion-Defect correlation for details). For each relative pdf, n = 50 (MDCK, WT), n = 61 (MDCK, mytomycin-c treatment), n = 85 (MCF10A), n = 79 (HaCaT). n = 30 different relative pdfs are calculated from different sets of random points. Data are represented as mean ± standard error of the mean (s.e.m.). **g,** Montage of phase contrast images of defect formation and extrusion (appearing as white halo) at defect. Scale bar, 10 μm. Red lines overlaid on the image (represented as black lines in bottom panel) are nematic directors. The blue dot and arrow represent the defect core and tail-to-head direction of +1/2 defect of interest.

Figure 2 | MDCK WT epithelia behaves as a 2D, extensile, active nematic liquid crystal.
Average yy-component and xy-component of the strain rate map around +1/2 defect in **a, b,** experiment (n = 2142) and **d, e,** simulation of active nematic liquid crystal. Color code is positive for stretching and negative for shrinkage. xx-component of strain rate map (not shown) is similar to the inverse of the yy-component of the strain rate map i.e. negative regions in yy-map are positive in xx-map and vice-versa. **c, f,** Corresponding average velocity flow field around +1/2 defect in experiment and simulation, respectively. **g,** Traction measurements around an extrusion at +1/2 defect on TFM gel (cyan dots - fiducial marker beads, arrows - traction force). Scale bar, 20 μm. **h,** Schematic of TFM setup to measure traction (t_x and t_y) and infer tissue stress (σ_{xx}, σ_{yy} and σ_{xy}). Comparison of average yy-component and xy-component of stress map around +1/2 defect between **i, j,** experiment and **k, l,** simulation, confirm the active nematic nature of the MDCK epithelia. Color code is positive for tensile stress and negative for compressive stress.(n = 1339). Overlaid black lines in panels show representative nematic directors, while grey circle denotes defect core.

Figure 3 | Compressive stresses at the head portion of +1/2 topological defects trigger cells extrusion.
Measurements of the average isotropic stress map around +1/2 and -1/2 defect in **a, b,** experiment and **c, d,** simulation demonstrate the mechanistic basis of correlation between cell extrusion and +1/2 defects based on compressive stresses at the head potion of +1/2 defects. Color code is positive for overall tensile state and negative for overall compression.(n = 1339 (+1/2 defect), n = 2454 (-1/2 defect)). Overlaid black lines in panels show representative nematic directors, while grey circle denotes defect core. **e,** Averaged temporal evolution of isotropic stress around cells (ROI of 65*65 μm^2) to be extruded at time = 0 min. (n = 44). Statistical analysis by t-test for each time point against a normal distribution centred at zero. Data are represented as mean ± s.e.m. *P < 0.05. **f,** Schematic of time evolution of tissue mechanical state before extrusion.

Figure 4 | Topologically induced +1/2 defects can control extrusion hotspots.
a, d, Confluent MDCK tissue confined on star and circle shape. Scale bar, 100 μm. Red lines overlaid on the images are nematic directors. **b, e,** Heat map of extrusion spatial frequency in respective confinement. **c, f,** Normalised probability distribution function (pdf) of extrusions, +1/2 defects and -1/2 defects as a function of distance from confinement centre, r_{fc}. Each point on the pdf is averaged over a full 360° for each specific range of r_{fc}. (n = 145 extrusions for star, n = 361 extrusions for circle). **g,** Schematic of laser induction of single cell apoptosis to check for potential effect of apoptotic factors on +1/2 defect numbers. **h,** Time evolution of the average number of +1/2 defects within radius of 80 μm around a single laser induced cell (laser induction at time = 0 min, n = 7 apoptotic induction experiments in different tissues). Statistical analysis by paired t-test for each time point against time = 0 min. Data are represented as mean ± s.e.m. **i,** Schematic of cell extrusion induced by nematic defect.

Extended Data Figure 1 | Further characterization of cell, tissue and extrusion-defect correlation properties.
a, b, Time evolution of cell aspect ratio and cell area in typical circularly confined MDCK epithelia. Data for each time point is binned over duration of 120 min. From lowest to highest time point, n = 5101, 5537, 5772, 6549, 6572, 6876, 6593 and 6831. Statistical analysis by t-test for each time point against time = 130 min. Data are represented as mean ± standard deviation (s.t.d.). $*P < 0.05$, $**P < 0.01$, $***P < 0.001$. **c,** Phase contrast image of MDCK monolayer on circular confinement (top). Red lines overlaid on tissue (represented again as black lines in middle panel) are nematic directors. Colour code shows the orientation of cells in the tissue (bottom). Scale bar, 100 μm. **d,** Time evolution of nematic measure (averaged local order parameter, S) of corresponding tissue (see Methods, Automated nematic characterization of experimental images for details). **e,** Schematic describing how correlation between extrusion and -1/2 defect is determined: the distance, r of each extrusion to its closest defect in the preceding frame is measured. **f,** Averaged relative probability distribution function (pdf) of r, for extrusion and -1/2 defect pairs compared to that of random point and -1/2 defect pairs (see Methods, Extrusion-Defect correlation for details). For each relative pdf, n = 50 (MDCK, WT), n = 61 (MDCK, mytomycin-c treatment), n = 85 (MCF10A), n = 79 (HaCaT). n = 30 different relative pdfs are calculated from different sets of random points. Data are represented as mean ± standard error of the mean (s.e.m.). **g,** Average measure of the strength of the extrusion-defect correlation i.e. sum of the two points closest to the origin in the relative pdf, for all conditions for +1/2 and -1/2 defects. n = 30 different relative pdfs are calculated from different sets of random points. Data are represented as mean ± standard error of the mean (s.e.m.). $*P < 0.05$, $**P < 0.01$, $***P < 0.001$.

Extended Data Figure 2 | Further examination of the identification of epithelia as extensile active nematics.
a, b, Average velocity flow field around +1/2 defect for mytomycin-c and blebbistatin treated MDCK. (n = 2003 (MDCK, mytomycin-c), n = 3061 (MDCK, blebbistatin)). **c,** Defect density (including + 1/2 and – 1/2 defects) for WT MDCK and blebbistatin treated MDCK. (n = 314 (MDCK, WT), n = 155 (MDCK, blebbistatin treatment)). Statistical analysis by t-test. Data are represented as mean ± s.e.m.

Extended Data Figure 3 | Spatial and temporal localization of defects with high compressive stress close to extrusions.
a, Heat map of the corresponding frequency of time and distances to the closest extrusions (for each defect group). +1/2 defects are grouped by the isotropic stress range at their head region. From negative (compressive) to positive (tensile)isotropic

stress groups. Color code 1 for highest frequency and 0 for no events. n = 1210, 1804, 4598, and 5929.

Extended Data Figure 4 | Automation of cell orientation and nematic defects detection.
Steps depicting automated nematic characterization of experimental images.

Fig. 1

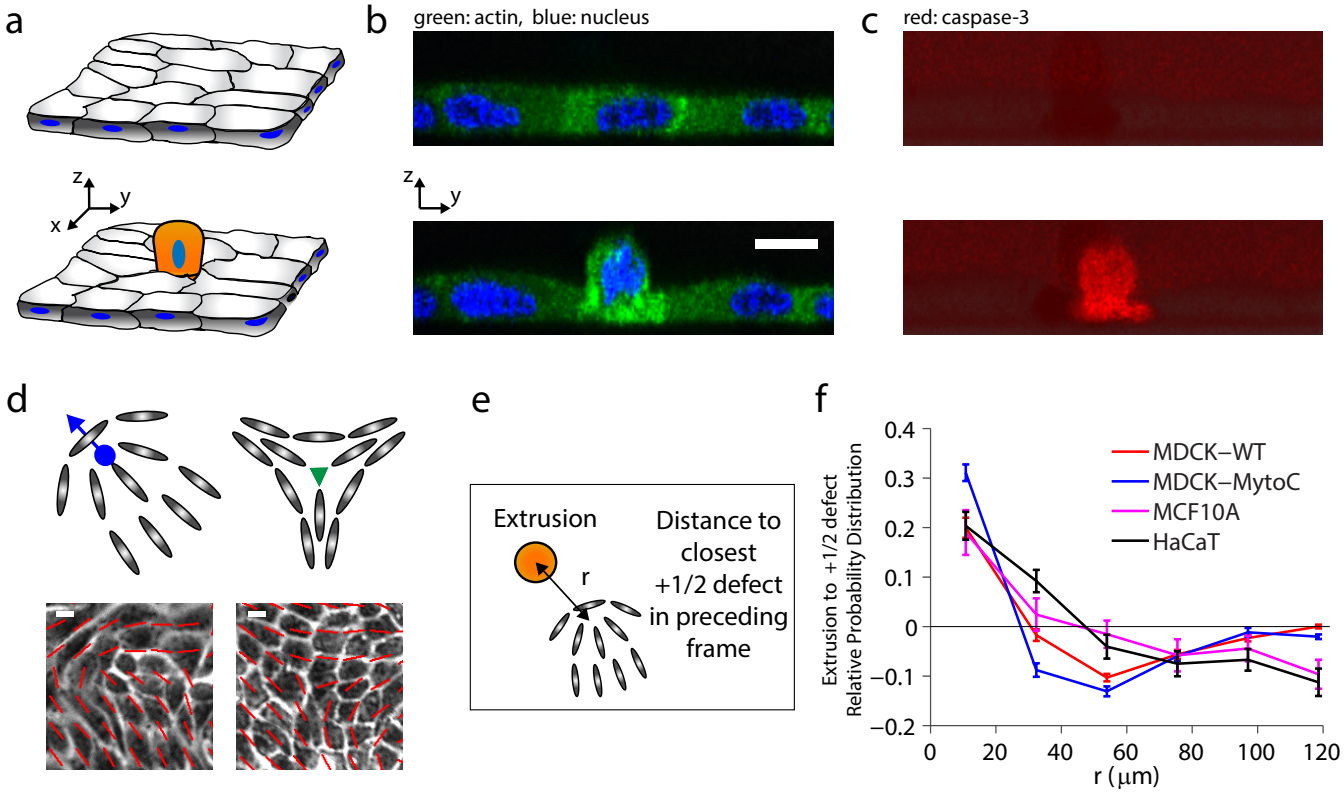
a
b
green: actin, blue: nucleus
c
red: caspase-3
z
y
x
z
y
d
e
Extrusion
r
Distance to closest +1/2 defect in preceding frame
f
Extrusion to +1/2 defect Relative Probability Distribution
0.4
0.3
0.2
0.1
0
−0.1
−0.2
0
20
40
60
80
100
120
r (μm)
MDCK–WT
MDCK–MytoC
MCF10A
HaCaT

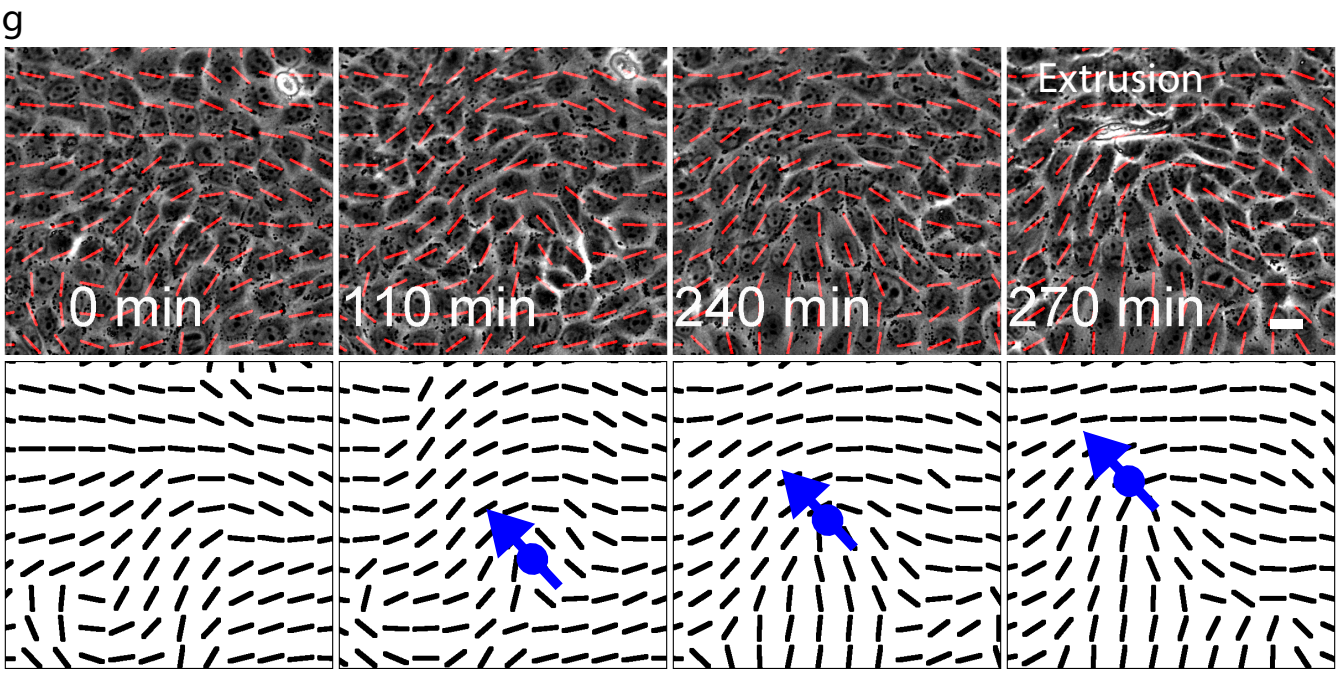
g
0 min
110 min
240 min
Extrusion
270 min

Fig. 2

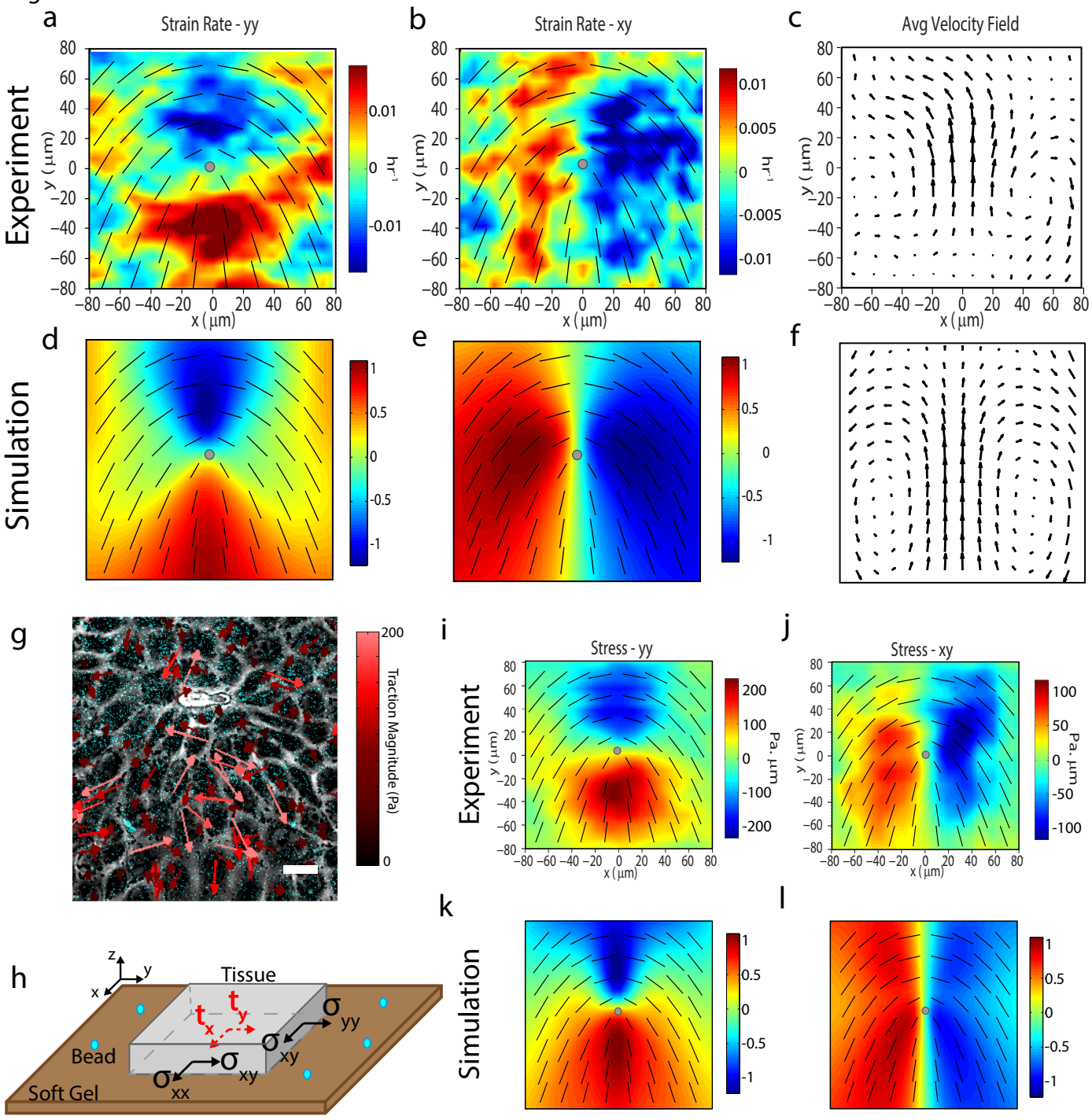
a
Strain Rate - yy
b
Strain Rate - xy
c
Avg Velocity Field
Experiment
Simulation
d
e
f
g
Traction Magnitude (Pa)
i
Stress - yy
j
Stress - xy
k
l
h
Tissue
Bead
Soft Gel
x (μm)
y (μm)
hr⁻¹
Pa. μm

Fig. 3

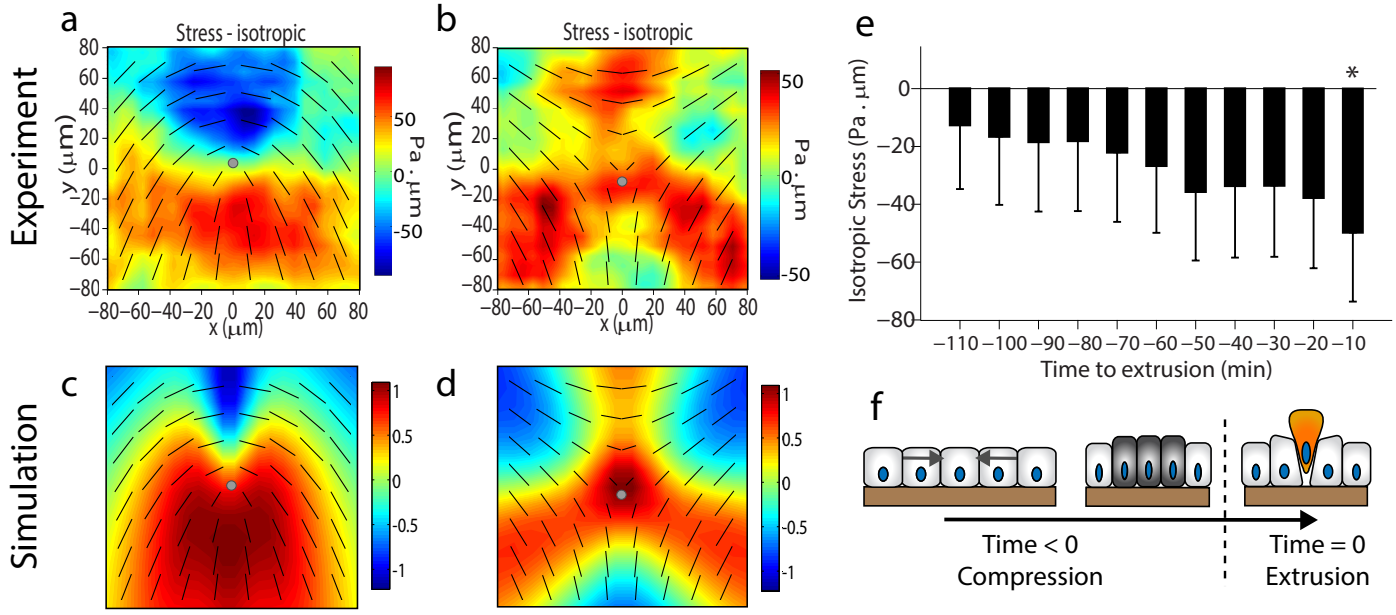
Experiment
Simulation
a
b
c
d
e
f
Stress - isotropic
Stress - isotropic
y (μm)
x (μm)
Pa . μm
Isotropic Stress (Pa . μm)
Time to extrusion (min)
*
Time < 0
Compression
Time = 0
Extrusion

Fig. 4

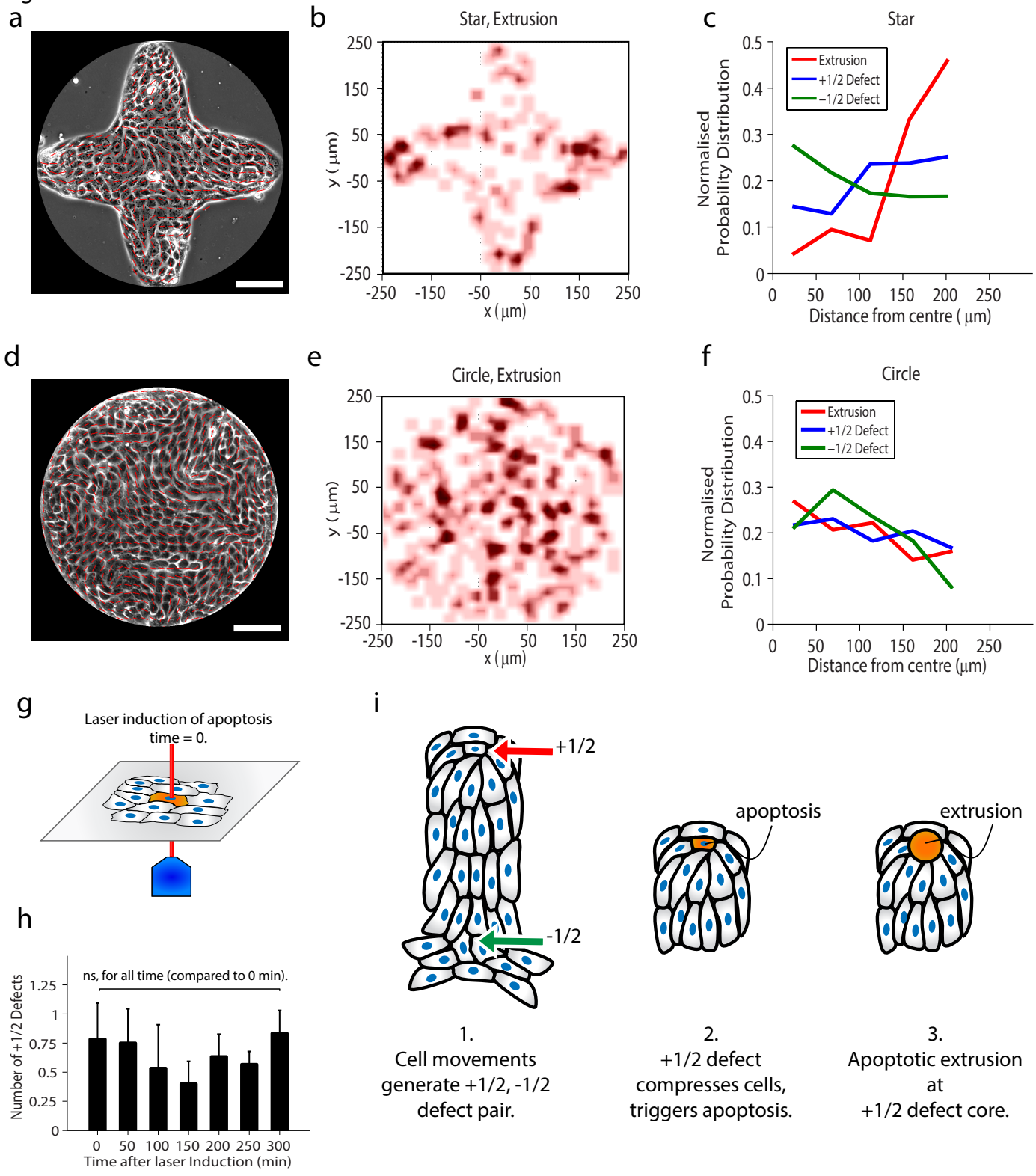
a
b
Star, Extrusion
y (μm)
x (μm)
c
Star
Extrusion
+1/2 Defect
−1/2 Defect
Normalised Probability Distribution
Distance from centre (μm)
d
e
Circle, Extrusion
f
Circle
g
Laser induction of apoptosis
time = 0.
h
ns, for all time (compared to 0 min).
Number of +1/2 Defects
Time after laser Induction (min)
i
+1/2
-1/2
apoptosis
extrusion
1.
Cell movements generate +1/2, -1/2 defect pair.
2.
+1/2 defect compresses cells, triggers apoptosis.
3.
Apoptotic extrusion at +1/2 defect core.